RSC Advances

PAPER

View Article Online
View Journal | View Issue

Cite this: *RSC Adv.*, 2022, **12**, 27492

Perovskite-structure $TlBO_3$ (B = Cr, Mn) for thermomechanical and optoelectronic applications: an investigation *via* a DFT scheme

Wakil Hasan,[a] Adeeb Mahamud Hossain,[a] Md. Rasheduzzaman,*[a] Md. Atikur Rahman,[b] Md. Mukter Hossain,*[c] K. Rashel Mohammad,[a] Raihan Chowdhury,[a] Khandaker Monower Hossain,[d] M. Moazzam Hossen[a] and Md. Zahid Hasan*[a]

First-principles-based DFT calculations have been carried out to analyze the structural, mechanical, elastic anisotropic, Vickers hardness, electronic, optical, and thermodynamic properties of $TlBO_3$ (B = Cr, Mn) for the first time. We determined the lattice parameters, which are in good agreement with the previous results. The Born criteria was ensured by the elastic constants, which also confirms the ductility of the solid. The elastic constants were also used to evaluate and analyze some related physical properties. The values of Vickers hardness were calculated to determine the hardness and relative application of both $TlCrO_3$ and $TlMnO_3$. Though the metallic characteristics were evaluated *via* the investigation of the electronic band structure and density of states, both $TlCrO_3$ and $TlMnO_3$ reveal semiconducting behavior under spin–orbit polarization with up-spin and down-spin configurations. Significant constants such as absorption, conductivity, reflectivity, dielectric, loss function, and refractive index were also considered and determined without spin and with spin. As a result, various possible electronic, optical, and optoelectronic applications were predicted. $TlBO_3$ (B = Cr, Mn) was also found to be reliable for thermal barrier coating (TBC) as indicated by the evaluated values of thermal conductivity and Debye temperature.

Received 11th July 2022
Accepted 8th September 2022

DOI: 10.1039/d2ra04273h

rsc.li/rsc-advances

1. Introduction

Perovskite oxides (ABO_3) are a point of interest for scientific researchers for their phase transformation and significant applications in modern technology.[1–5] ABO_3-structured perovskites have been extensively explored for metal-insulator transitions (MITs) correlated transition metal oxides.[6–14] $La_{1-x}B_xMnO_3$(B = Mn, Ca) perovskite magnates are well known to show MITs with ferromagnetic–paramagnetic transition.[15] Perovskite materials are also found to be suitable for solid oxide fuel cells.[16,17] ABO_3 is considered as an ideal perovskite material, where A is a monovalent otherwise divalent cation situated on the edges of the crystal, and B is a tetravalent or pentavalent transition metal.[18,19] Kim *et al.* discussed the structural distortion of ABO_3-type perovskite owing to a disparity in the A–O and B–O bond distances.[20] The physical properties of A cation on structural distortion are difficult to investigate, as Kim *et al.* agreed, because rare earth and yttrium ions bond to oxygen with parallel covalency. As a result, Tl(III), a post-transition metal ion, is a decent choice for A cation in ABO_3 perovskites due to its full occupation of the 4f and 5d orbitals ([XE] = $4f^{14}$ $5d^{10}$ $6s^2$ $6p^1$) in comparison to rare-earth ions ([XE] = $4f^n$ $5d^0$ $6s^0$; $0 \leq n \leq 14$). The transition metals in the B site of ABO_3 perovskite make the material suitable for any application such as high-temperature superconductivity, colossal magnetoresistance (CMR), charge ordering, giant magnetoresistance (GMR), piezoelectricity, and ferroelectricity.[21–24] ABO_3 perovskite oxides are also interesting because of their use in the construction of infrared sensors, optoelectronic modulators, infrared detectors, microwave devices, and different electromechanical systems.[25–28] Tl(III) compounds such as $TlFeO_3$ and $TlCrO_3$ were formulated five decades back[29] but lack in-depth investigation due to the difficulty of their preparation. Thus, it is exciting to further study $TlBO_3$ (B = Cr, Mn)-structured perovskites.

$ACrO_3$ (A = Sc, I, Tl, Bi)[30–34] perovskite-type chromite is significantly different in its properties from isostructural chromite $RCrO_3$ (R = rare earth elements), which can result from the distortion of the crystal structure ($ScCrO_3$, $InCrO_3$), chemical bonds ($TlCrO_3$, $BiCrO_3$) in these compounds, and the electronic structure of A^{3+}.[35] $RCrO_3$ compounds have been found to exhibit spin reorientation transition, good oxygen-ion conduction

[a]*Department of Electrical and Electronic Engineering, International Islamic University Chittagong, Kumira, Chittagong 4318, Bangladesh. E-mail: rashedbscm@gmail.com; zahidhasan.02@gmail.com*

[b]*Department of Physics, Pabna University of Science and Technology, Pabna 6600, Bangladesh*

[c]*Department of Physics, Chittagong University of Engineering and Technology (CUET), Chattogram 4349, Bangladesh. E-mail: mukter_phy@cuet.ac.bd*

[d]*Department of Materials Science and Engineering, University of Rajshahi, Rajshahi 6205, Bangladesh*

(doped), and sensitivity toward methanol, ethanol, some gases, and humidity.[36] $R^{3+}Mn^{3+}O_3$ have also been investigated for their multiferroic properties in both perovskites and hexagonal modification[37–42] and rich magnetic phases.[41] $RCrO_3$ (R = Gd, Tb, Er, Tm, Sn, and Y)[43,44] has shown large polarization at a high temperature equivalent to the Neel temperature (T_N) of the Cr subsystem, while $LaCrO_3$ and $CeCrO_3$ display high T_N in $RCrO_3$ structure type materials.[45] Orthorhombic $RMnO_3$ (R = Tb, Dy)[37,46] are spiral magnets that display magnetoelectric (ME) coupling. $DyFeO_3$ was investigated by Tokunaga *et al.* and found to be versatile with gigantic ME phenomena.[47]

Paul *et al.* analyzed ABO_3 perovskites such as $BiNiO_3$ or $PbCrO_3$ (ref. 48) for MITs, and different investigations on A and B ions led to the proposition of two more candidates in this category, namely, $TlMnO_3$ and $InMnO_3$. Yi *et al.* synthesized $TlCrO_3$ (ref. 31) and $TlMnO_3$ (ref. 49) and investigated them with Mössbauer spectroscopy with high pressure (6 GPa) and high temperature (1500 K), and found separate structural and magnetic properties, where the absence of spin canting suggested that $TlCrO_3$ has a non-trivial magnetic structure. Khalyavin *et al.* also studied the magnetic structure of $TlMnO_3$ (ref. 50) under the same conditions of high temperature and pressure by applying the neutron diffraction technique and confirmed anisotropic exchange interactions that revealed that the Jahn–Teller distortion plays a key role in creating the magneto-crystalline anisotropy. Belik investigated manganese oxide-based $Bi_{1-x}Y_xMnO_3$ with high pressure and high temperature.[51] R_2O_3–In_2O_3 systems were studied at normal pressure, and some ABO_3 compounds were found that contained I^{3+} or Tl^{3+}.[52,53] With this criteria, Shannon synthesized some perovskites containing In and Tl such as $InCrO_3$, $TlCrO_3$, and $TlFeO_3$.[29] *Ab initio* study was performed on many perovskites including $BaMO_3$ (M = Pr, Th, U),[54] $SnTaO_3$,[21] ACO_3 (A = Ca, Sr),[55] and $SrHfO_3$.[56] Z. Hasan *et al.* investigated the ABO_3 type perovskite $AMoO_3$,[57] where A is Ca, Sr, $SrBO_3$ (ref. 58) and B is Cr, Fe, and $SrFeO_3$,[59] with density functional theory (DFT) and found them to be mechanically stable at different pressures along with other physical properties. $LnCrO_3$,[60–62] which crystallizes in $GdFeO_3$ and $BiFeO_3$ with similar structured perovskites, were studied and found to have applications in thin-film devices. $LaNiO_3$ reveals a metallic nature along with Pauli paramagnetism. $LuNiO_3$ and $YNiO_3$, on the other hand, display Curie–Weiss paramagnetism with antiferromagnetic order, which is below the T_N.[63] The $TlNiO_3$ perovskite was synthesized under high pressure and a relative study was performed with $TNiO_3$ (T = rare earth).[64] According to Cao *et al.*, chromium oxide-based $CeCrO_3$,[65] which is a rare earth orthochromite, shows magnetic properties and anti-ferromagnetism. $LaCoO_3$ with ABO_3 structure was studied for a lengthy period for its spin-state transition and electronic or ionic conductivity.[66] Mn^{3+}-based perovskite $TlMnO_3$ has been described to have a triclinic crystal structure with a clear signature of Jahn–Teller distortion.[49] Ding *et al.* investigated $TlCrO_3$, $InCrO_3$, and $ScCrO_3$ with high pressure and high-temperature settings, which revealed the orthorhombic structure of these materials.[67]

In this study, further investigation of the ABO_3 structure-based $TlBO_3$ (B = Cr, Mn) is done, where Tl is a post-transition metal, Cr and Mn are transition metals, and O is a non-metal. ABO_3 structure-based perovskite shows unique physical properties whose diverse types are used in modern technology, motivating us to properly analyze and uncover their physical properties. This paper studies the physical properties such as structural, mechanical, elastic anisotropic, electronic, thermal, Vickers hardness, and optical properties of $TlCrO_3$ and $TlMnO_3$ compounds using DFT-based CAmbridge Serial Total Energy Package (CASTEP). The main purpose of this investigation is to analyze the abovementioned physical properties of the perovskites that can be subjugated to different usages.

2. Computational methods

The investigation of various physical properties such as structural, electronic, mechanical, thermal and optical $TlBO_3$ (B = Cr, Mn) were done with the most commonly used first-principles method. Density Functional Theory (DFT) with the periodic ambient condition along with generalized gradient approximation (GGA) and Perdew–Burke–Ernzerhof (PBE) exchange-correlation functional was employed[68–70] using the Cambridge Serial Total Energy Package (CASTEP) code.[71] The atomic calculations for Tl – $6s^2\ 6p^1$, Cr – $3d^5\ 4s^1$, Mn – $3d^5\ 4s^2$, and O – $2s^2 2p^6$ were executed. Brillouin zone *k*-points sampling was done using the Monkhorst–Pack scheme[72] with $10 \times 7 \times 10$ grid points for $TlCrO_3$ and $7 \times 5 \times 7$ grid points for $TlMnO_3$. The plane-wave cut-off energy was 450 eV and 400 eV for $TlCrO_3$ and $TlMnO_3$, respectively. The Broyden–Fletcher–Goldfarb–Shanno (BFGS) minimization method, also known as the quasi-Newton method,[73] was employed as a method of optimization of the crystal. The principles of convergence for the optimization were set to 1×10^{-5} eV per atom for total energy, 0.03 eV $Å^{-1}$ for maximum force, and 0.05 GPa for maximum stress. The stress–strain method[74] was used to attain the elastic stiffness constants of $TlBO_3$ (B = Cr, Mn) using CASTEP. The Young's modulus, shear modulus, and Poisson's ratio presented in the 3D anisotropy models were obtained using the ELATE program.[75] Lastly, the electronics properties were evaluated by setting the abovementioned parameters.

3. Results and discussion

3.1 Structural properties

Both synthesized $TlBO_3$ (B = Cr, Mn) perovskite materials share the same $TlBO_3$ ionic structure but both share different crystal structure types. Fig. 1 illustrates the crystal structure of $TlBO_3$ (B = Cr, Mn). $TlCrO_3$ crystallizes in an orthorhombic structure in the space group *Pnma* (no. 62). In $TlCrO_3$, the Tl site has 4c Wyckoff position (0.04617, 0.25, 0.98732), the Cr site has 4b Wyckoff position (0, 0, $\frac{1}{2}$), and O has two sites, for the first one, the 4c Wyckoff position (0.4504, 0.25, 0.1050) and for the second, the 8d Wyckoff position (03 009, 0.0558, 0.6969).[31] $TlMnO_3$ crystalizes in the triclinic structure with the space group $P\bar{1}$ (no. 2). In $TlMnO_3$, Tl site has 2i (0.54745, 0.25794, 0.50994) and 2i (0.04935, 0.24233, 0.97513). The Mn atoms are positioned in 4 sites. Mn1, Mn2, Mn3, and Mn4 has 1d (1, 0.5, 0, 0), 1e (1, 0.5, 0.5, 0). 1b (1, 0, 0, 0.5), and 1g (1, 0, 0.5, 0.5),

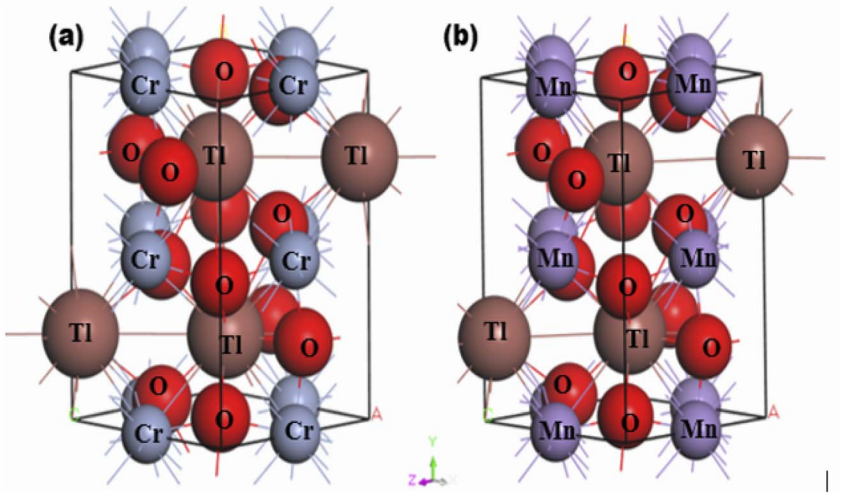

Fig. 1 Crystal structures of (a) $TlCrO_3$ and (b) $TlMnO_3$.

respectively. O atoms are positioned in 6 site O (1–6), which are in the numerical order as follows—2i (for all sites) Wyckoff position (0.9423, 0.2309, 0.3799); (0.4450, 0.2708, 0.1147); (0.2056, 0.5732, 0.2055); (0.8053, 0.0511, 0.8070); (0.2824, 0.4406, 0.6847); (0.6839, 0.9275, 0.2855), respectively.[49] The optimized lattice parameters *a*, *b*, and *c* are presented in Table 1 along with the calculated unit cell volume *V*. The obtained results are associated with the former results and seems to be in good agreement with them, which shows our calculations to be reliable. It is noted that both materials share different crystals structures, but the calculated lattice constants and volumes are quite close.

3.2 Elastic constants and mechanical properties

The elastic characteristics of a crystal define various features of the solid under symmetry conditions, as well as solid stability, bonding characteristics, elastic, and machinability.[77] The elastic constants are produced from the first approach *via* the CASTEP module using a variety of uniform finite value distortions. After the optimization of the internal degrees of freedom, the stresses are therefore determined.[78] The elastic constants for $TlBO_3$ (B = Cr, Mn) were determined and are presented in Table 2. Nine elastic constants were calculated for orthorhombic $TlCrO_3$ and twenty-one elastic constants were found for triclinic $TlMnO_3$. No past results regarding elastic constants were found; thus, no relative investigation has been shown. The current outcomes (elastic constants) must adhere to the Born stability principles by describing the following relationships.

$$C_{11} - C_{12} > 0,\ C_{44} > 0, \text{ and } C_{11} + 2C_{12} > 0 \quad (1)$$

The elastic constants calculated are positive (Table 2) and uphold the abovementioned stability criteria, which confirms the mechanical stability of $TlBO_3$ (B = Cr, Mn). The material also satisfies generalized stability criteria for an orthorhombic crystal ($TlCrO_3$),[71,79,80] which is as follows.

$$C_{ij} > 0,\ (ij = 1\text{–}6); \quad (2)$$

$$[C_{11} + C_{22} + C_{33} + 2\,(C_{12} + C_{13} + C_{23})] > 0; \quad (3)$$

$$[C_{11} + C_{22} - 2C_{12}] > 0; \quad (4)$$

$$[C_{13} + C_{33} - 2C_{13}] > 0; \quad (5)$$

$$[C_{22} + C_{33} - 2C_{23}] > 0; \quad (6)$$

Table 1 Calculated lattice constants and unit cell volume of $TlBO_3$ (B = Cr, Mn)

	Lattice constants (Å)				
Compound	*a*	*b*	*c*	Volume (Å^3)	Remarks
$TlCrO_3$ (orthorhombic)	5.433306	7.693412	5.434486	227.16511	This work
	5.40318	7.64699	5.30196	219.06671	Exp.[31]
	5.405	7.647	5.302	219.14245	Exp.[29]
$TlMnO_3$ (triclinic)	5.457218	7.692286	5.463322	229.341717	This work
	5.4248	7.9403	5.28650	227.713553	Exp.[49]
	5.41987	7.9250	5.27683	226.652881	Exp.[50]
$LaCrO_3$ (orthorhombic)	5.6139	7.8942	5.5702	246.856	Exp.[76]
$LaMnO_3$ (orthorhombic)	5.765	7.582	5.5702	237.302	Exp.[76]

Table 2 Elastic constants, C_{ij} (GPa) of $TlBO_3$ (B = Cr, Mn)

$TlCrO_3$ (orthorhombic)		$TlMnO_3$ (triclinic)			
C_{11}	298.487	C_{11}	247.771	C_{23}	144.011
C_{22}	252.195	C_{22}	219.456	C_{24}	−0.484
C_{33}	298.712	C_{33}	298.029	C_{25}	1.908
C_{44}	104.875	C_{44}	87.156	C_{26}	−1.104
C_{55}	42.099	C_{55}	35.395	C_{34}	−3.159
C_{66}	104.859	C_{66}	74.132	C_{35}	2.344
C_{12}	150.459	C_{12}	131.126	C_{36}	−0.291
C_{13}	85.594	C_{13}	110.109	C_{45}	−1.427
C_{23}	150.071	C_{14}	−6.898	C_{46}	1.183
		C_{15}	0.171	C_{56}	1.436
		C_{16}	−1.434		

The elastic constants of the compound in Table 2 agree with the above conditions, further confirming that the considered compound $TlCrO_3$ is mechanically stable in the orthorhombic phase. For both the materials, the C_{44}, C_{55}, and C_{66} crudely agree with the distortions of the lattice angles (α, β, and γ). It can be concluded that γ is the maximum stable angle since the elastic constant C_{66} is larger than C_{44}/C_{55} (Table 2), which is dependent on the changing tendencies of the lattice angles in the crystal.[81] Here, C_{11} is connected with linear compression resistance in the *x*-direction and the value C_{11} is higher than C_{12}, which indicates incompressibility near the *a*-axis, not near the *b*-axis. The density of the atom along the [100] direction is higher if compared with the direction of [011]. It is also seen that $C_{44} > C_{66}$ for $TlMnO_3$, which means higher shear deformation resistance along the [010] direction than the [110] direction, while for the $TlCrO_3$ compound, this value is not so different. The shear component, C_{44} ($TlCrO_3$) > C_{44} ($TlMnO_3$), indicating higher resistance to shear deformation of $TlCrO_3$ compared to $TlMnO_3$. Furthermore, the value of C_{44} predicts the hardness of the material. Therefore, it assumes that the compound $TlCrO_3$ should have higher hardness than $TlMnO_3$. From Cauchy pressure (C_{12}–C_{44}) the metallic or non-metallic (ionic/covalent) features of the compounds are revealed. The materials will be a dominant covalent bond in nature if the Cauchy pressure shown in Table 3 is negative, which is not the case. Thus, both $TlCrO_3$ and $TlMnO_3$ have a dominant ionic bond in nature as the Cauchy pressure values are positive.

Voigt–Reuss–Hill (VRH) approximations are employed to evaluate the polycrystalline elastic properties.[82–84] Bulk modulus (B_V) and shear modulus (G_V) in Voigt approximation is expressed as follows.

$$B_V = 1/9\ [(2(C_{11} + C_{12}) + 4C_{13} + C_{33})]; \quad (7)$$

$$G_V = 1/30\ (C_{11} + C_{12} - 4C_{13} + 12C_{44} + 12C_{66}); \quad (8)$$

The Bulk modulus B_R and shear modulus G_R in the Reuss approximation is defined as follows.

$$B_R = \frac{C^2}{M};\ C^2 = (C_{11} + C_{12})C_{33} - 2C_{13}{}^2; \quad (9)$$

$$M = C_{11} + C_{12} + 2C_{33} - 4C_{13}; \quad (10)$$

$$G_R = \frac{\frac{1}{2}[5C^2C_{44}C_{66}]}{3B_VC_{44}C_{66} + C^2(C_{44} + C_{66})};\ C_{66} = \frac{C_{11} - C_{12}}{2} \quad (11)$$

For Hill approximation, *B* and *G*, which are bulk and shear modulus, respectively, are calculated utilizing the following equations.

$$B = \frac{1}{2}(B_V + B_R); \quad (12)$$

$$G = \frac{1}{2}(G_V + G_R); \quad (13)$$

As we know, the elastic moduli bulk modulus *B*, shear modulus *G*, Young's modulus *Y*, and Poisson's *v* describe the mechanical performance of solids, which are calculated by VRH approximations.[85–87] *B* and *G* is then used to determine the Young's modulus *Y* and Poisson's ratio *v via* the following equations.[88]

$$Y = \frac{9BG}{3B + G}; \quad (14)$$

$$v = \frac{3B - 2G}{2(3B + G)}; \quad (15)$$

The resistance in contradiction to volume, shear, and longitudinal deformation is represented by bulk modulus *B*, shear modulus *G*, and Young's modulus *Y*, respectively. *Y*, *G*, and *B* of $TlBO_3$ were determined for the first time in this investigation and are shown in Table 3. Pugh's ratio, depicted as *B*/*G*, in Table 3 demonstrates if a material is ductile or brittle,[89]

Table 3 The estimated bulk modulus, B_R (Reuss), B_V (Voigt), *B* (Hill) (GPa), shear modulus, G_R (Reuss), G_V (Voigt), *G* (Hill) (GPa), Young's modulus, *Y* (GPa), Pugh's ratio, *B*/*G*, Poisson's ratio *v*, Cauchy pressure, C_{12}–C_{44}, and machinability index μ_M of $TlBO_3$ (B = Cr, Mn)

Elastic moduli and mechanical properties												
Compound	B_R	B_V	*B*	G_R	G_V	*G*	*Y*	*B*/*G*	*v*	C_{12}–C_{44}	μ_M	Remarks
$TlCrO_3$ (orthorhombic)	179.92	180.18	180.05	68.39	81.25	74.82	197.12	2.41	0.32	45.58	1.72	This work
$TlMnO_3$ (triclinic)	168.62	170.64	169.63	56.79	64.67	60.73	162.76	2.79	0.34	43.97	1.93	This work
$CeCoO_3$ (cubic)	179.12	179.12	179.12	72.66	80.39	76.53	200.97	2.34	0.32	45.12	3.05	Exp.[92]
$CeCuO_3$ (cubic)	132.09	132.09	132.09	39.94	46.55	43.24	116.96	3.05	0.35	54.51	4.25	Exp.[92]

which is more than 1.75, indicating the ductile nature of both the materials; otherwise, it behaves in a brittle manner. Likewise, Poisson's ratio ν is an additional parameter to determine the ductile or brittle nature of solids.[90] The value should be more than 0.25 to be ductile and less to be brittle. As the value of ν is more than 0.25, as shown in Table 3, it further confirms the result obtained from Pugh's ratio, suggesting that both $TlCrO_3$ and $TlMnO_3$ are ductile. Furthermore, the value of the Cauchy pressure (C_{11}–C_{44}) is positive, indicating the ductile nature of both materials; otherwise, it would be brittle if the value is negative.[91]

The machinability index μ_M describes the cutting capability of a compound, the maximum financial level of machine operation, and plastic strain, which is vital for industrial areas. It is determined as follows.

$$\mu_M = \frac{B}{C_{44}}. \tag{16}$$

For both orthorhombic $TlCrO_3$ and $TlMnO_3$, the value of μ_M in Table 3 is more than 2, referring to improved lubricating characters and lesser frictions, which has significant applications in different fields.

3.3 Elastic anisotropy

The microscopic activity of solids is developed by the amount of elastic anisotropy for single and polycrystalline materials.[93] Therefore, the investigation of the outward directional dependence of the elastic tensor is important for the materials involved so that the mechanical resilience, degree of elastic anisotropy, and usage of material under peripheral stress can be heightened. In applied engineering sciences, these appearances will play an equally critical part in the design activities, clear interpretations, along with fundamental crystal physics.[94] The Shivakumar Ranganathan model represents elastic anisotropy as follows.[83]

$$A^U = 5\frac{G_V}{G_R} + \frac{B_V}{B_R} - 6 \geq 0. \tag{17}$$

$A^U = 0$ represents the isotropic performance, although the exemption from this ($A^U \neq 0$) replicates the anisotropic performance of materials. Therefore, the values of A^U are estimated for orthorhombic $TlCrO_3$ (~0.941) and triclinic $TlMnO_3$ (~0.702), characterizing both materials as anisotropic. Furthermore, Chung and Buessum presented the conception of percent anisotropy modulus, A_G (shear), and A_B (bulk) as follows[82] (in polycrystalline materials).

$$A_G = \frac{G_V - G_R}{2G_H}; \quad A_B = \frac{B_V - B_R}{B_V + B_R}. \tag{18}$$

For $A_G = A_B = 0$, the solid materials represent elastic isotropy. Thus, in the present analysis, both $TlCrO_3$ and $TlMnO_3$ show anisotropic aspects. If we consider the directional requirement on the elastic tensor, $TlMnO_3$ shows a higher degree of anisotropy. In addition, shear anisotropy is more prevalent as it seems to have a greater value (Table 4) for both the materials. In both the materials, $TlBO_3$ (B = Cr, Mn) the bulk modulus is anisotropic, as we observed that $B_H \neq B_R \neq B_V$. The value of A_B in Table 4 illustrates that the bulk modulus of compounds is anisotropic and $TlMnO_3$ is further anisotropic than $TlCrO_3$, which shows negligible anisotropic character. Both compounds indicate anisotropic character (Table 4) in the measured shear anisotropic factors as well. The anisotropic shear pointers offer a valuation of the degree of anisotropy in the bonding of different planes between atoms. Along the {100}, {010}, and {001} shear planes, the shear anisotropic parameters are stated as follows.

$$\begin{aligned} A_1 &= \frac{4C_{44}}{C_{11} + C_{33} - 2C_{13}}; \\ A_2 &= \frac{4C_{55}}{C_{22} + C_{33} - 2C_{23}}; \\ A_3 &= \frac{4C_{66}}{C_{11} + C_{22} - 2C_{12}}. \end{aligned} \tag{19}$$

In the case of $A_1 = A_2 = A_3$, the materials show isotropic nature or it measures the amount of elastic anisotropy exhibited by the crystal. Since A_1, A_2, and A_3 are not equivalent (Table 4), both orthorhombic and triclinic materials display anisotropic character. The Zener anisotropy index (A) and the Zener anisotropy equivalent (A^{eq}) for both the compounds are calculated to achieve acceptable anisotropy as follows.[95,96]

$$A = \frac{2C_{44}}{C_{11} - C_{12}}, \tag{20}$$

$$A^{eq} = \left(1 + \frac{5}{12}A^U\right) + \sqrt{\left(1 + \frac{5}{12}A^U\right)^2 - 1}. \tag{21}$$

In Table 4, the values of A and A^{eq} confirm our previous analysis, reinstating that both the compounds have an anisotropic character. The anisotropy index $A = 1$ suggests the isotropic behavior of solid materials, and anisotropic natures are revealed for more or less than Uni (>1 or <1). The evaluated value of $TlBO_3$ (B = Cr, Mn) shows both materials to be anisotropic, where $TlCrO_3$ manifested a slightly higher degree of elastic anisotropy.

To further study the elastic anisotropy of both the materials, Young's modulus (Y), bulk modulus (K), shear modulus (G), and

Table 4 Calculated shear anisotropic factors, A_i (i = 1–3), Zener's anisotropy index (A), anisotropy in shear (A_G), anisotropy in bulk modulus (A_B), universal anisotropy index (A^U), and equivalent Zener anisotropy (A^{eq}) of $TlBO_3$ (B = Cr, Mn)

Compound	Crystal system	A_1	A_2	A_3	A	A_G	A_B	A^U	A^{eq}
$TlCrO_3$	Orthorhombic	0.985	0.672	1.679	1.417	0.086	0.0007	0.941	2.3605
$TlMnO_3$	Triclinic	1.071	0.617	1.447	1.494	0.065	0.0059	0.702	2.1114

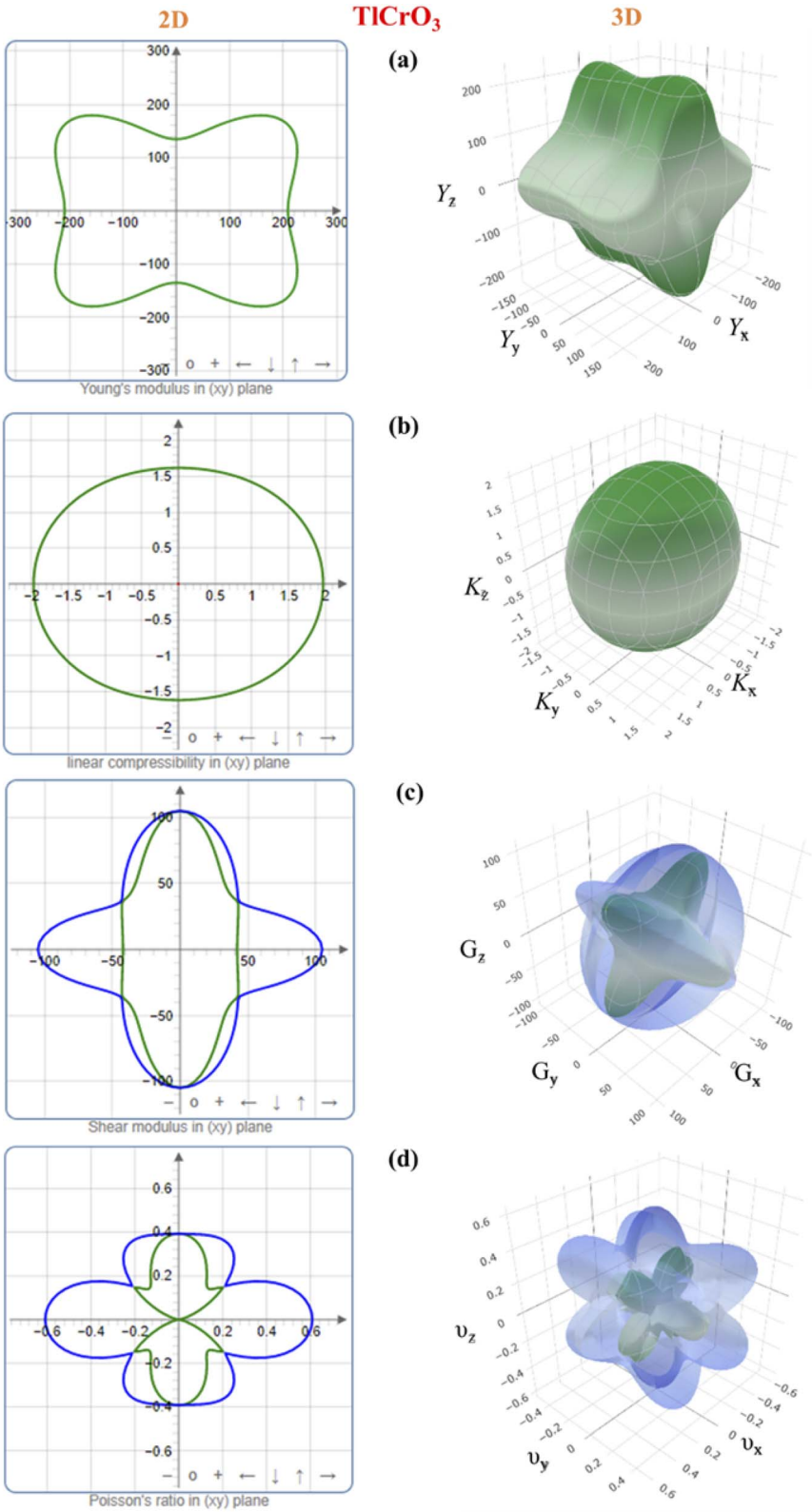

Fig. 2 3D and 2D anisotropy contour plots of (a) Young's modulus, *Y*, (b) compressibility, *K*, (c) shear modulus, *G*, and (d) Poisson's ratio, *v* of $TlCrO_3$.

Poisson's ratio (ν) elastic moduli were constructed for both $TlCrO_3$ and $TlMnO_3$ in Fig. 2 and 3 using ELATE code.[75] 3D and 2D models were used to identify the nature of anisotropy. If the 3D plots are entirely spherical and their projection on different planes is rounded, the materials are isotropic. The non-spherical shape in the 3D plots for both orthorhombic $TlCrO_3$

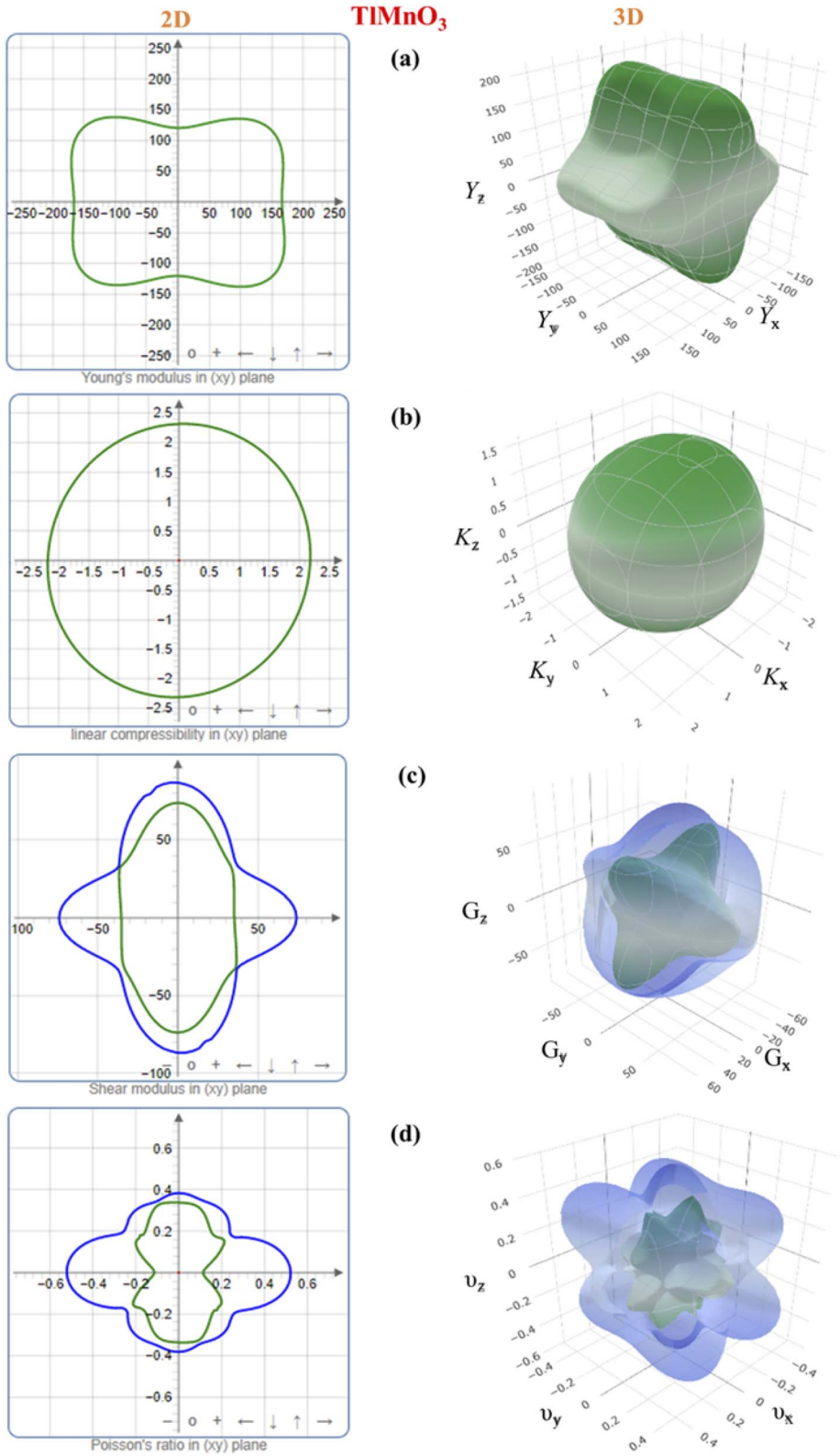

Fig. 3 3D and 2D anisotropy contour plots of (a) Young's modulus, *Y*, (b) compressibility, *K*, (c) shear modulus, *G*, and (d) Poisson's ratio, *v* of $TlMnO_3$.

and triclinic $TlMnO_3$ signify the extent of anisotropy. As depicted in Fig. 2 and 3, the unconventionality between the 3D surface and the sphere for all the moduli suggests the elastic anisotropy characteristics for $TlBO_3$ (B = Cr, Mn). This analysis displays good consistency with the results of all the anisotropy indexes discussed above. Furthermore, the 3D plot of different

anisotropy moduli looks somewhat similar in Fig. 2 and 3 for both the compounds.

3.4 Vickers hardness

Vickers hardness is mainly associated with the resistance offered by the material to plastic deformation. The ability of a material to resist plastic deformation can also be estimated by it. Many important applications for practical devices can be predicted by understanding the hardness of a solid. Furthermore, a deep understanding of the mechanical behavior can be achieved through the relationship between elastic polycrystalline modules and hardness. Vickers hardness can be calculated for metallic compounds by the means of the equation found by Gou *et al.*[97] If all the individual bond hardness are calculated, their geometric average can be used to evaluate the hardness of a multiband solid. It can be done using the following equations.[98–100]

$$H_V = \left[\prod \pi\left(H_v^{\mu}\right)^{n^{\mu}}\right]^{1/\sum n^{\mu}} \quad (22)$$

$$H_v^{\mu} = 740(P^{\mu} - P^{\mu'})(\upsilon_b^{\mu})^{-5/3}; \quad (23)$$

$$P^{\mu'} = \frac{n_{\text{free}}}{V}; \quad (24)$$

$$n_{\text{free}} = \int_{E_p}^{E_F} N(E)\mathrm{d}E \quad (25)$$

$$\upsilon_b^{\mu} = \frac{(d^{\mu})^3}{\sum_{\upsilon}\left[(d^{\mu})^3 N_b^{\upsilon}\right]} \quad (26)$$

here, $P^{\mu'}$ and P^{μ} is the Mulliken population and the metallic population of the μ-type bond, respectively, n_{free} is the number of free electrons between the first pseudo gap and Fermi level, V is called cell volume (Table 1), υ_b^{μ} is the volume of a bond of μ-type, $(d^{\mu})^3$ is the bond length of μ-type bond, and N_b^{υ} is the bond number of υ per unit volume.

The evaluated values of Vickers hardness of $TlBO_3$ (B = Cr, Mn) are displayed in Table 5. It is clear from Table 5 that $TlCrO_3$ is harder than $TlMnO_3$. However, the overall observation of the values reveals both materials to have much lower hardness compared to diamond, considering the most rigid (Vickers hardness 70 to 150 GPa)[101] material among all. As a result, both $TlCrO_3$ and $TlMnO_3$ indicate a flexible and soft nature, making them suitable for thin-film production. The hardness values are 8.729 GPa for $TlCrO_3$ and 5.208 Gpa for $TlMnO_3$, which is close to 2–8 GPa, values of many well-known MAX phase (M is transition metal, A is group 13–15 A element, X is C or N) materials.[102]

3.5 Electronic properties

The electronic properties of the $TlBO_3$ (B = Cr, Mn) perovskites were studied by measuring the band structure along with the total partial density of states (DOS). The electronic band structures without spin for both orthorhombic $TlCrO_3$ and triclinic $TlMnO_3$ are displayed in Fig. 4(a) and 5(a) correspondingly. The band structure with spin is displayed in Fig. 4(a) and 5(a). The straight (dotted) line at 0 eV in both Fig. 4 and 5 specifies the Fermi level (E_F) separating the conduction band and the valence band. If the electronic band-structure of both the materials is compared, it is observed that for both materials, energy bands without spin display bulky scattering diagonally to the Fermi level (E_F); the conduction and valence bands both are superimposed and displayed no bandgap, suggesting both materials to be metals. Moreover, the energy density of $TlMnO_3$ along the Fermi level (E_F) describes it to be more metallic than $TlCrO_3$. The bandgap ($E_g = 0.45$) in Fig. 5(a) reveals possible semiconducting abilities in $TlMnO_3$. Then again, the band structure with spin shows a dramatic transition from metallic to semiconductor for

Table 5 Theoretical hardness of $TlBO_3$ (B = Cr, Mn)

Compounds	Bond	n^{μ}	d^{μ} (Å)	P^{μ}	$P^{\mu'}$	υ_b^{μ} (Å^3)	H_v^{μ} (GPa)	H_v (GPa)
$TlCrO_3$	O–Cr(I)	8	1.9201	0.55	0.043743	9.43794	8.888 053	8.72858
	O–Cr(II)	8	1.92232	0.54	0.043743	9.47072	8.662 297	
	O–Cr(III)	8	1.92342	0.54	0.043743	9.48698	8.637 555	
$TlMnO_3$	O–Mn(I)	2	1.95981	0.36	0.071407	5.04956	14.36908	5.20793
	O–Mn(II)	2	1.96337	0.36	0.071407	5.07713	14.23928	
	O–Mn(III)	2	1.96358	0.36	0.071407	5.07876	14.23167	
	O–Mn(IV)	2	1.96733	0.35	0.071407	5.10791	13.60809	
	O–Mn(V)	2	1.9818	0.35	0.071407	5.22145	13.1185	
	O–Mn(VI)	2	1.98243	0.35	0.071407	5.22643	13.09767	
	O–Mn(VII)	2	1.98378	0.35	0.071407	5.23711	13.05316	
	O–Mn(VIII)	2	1.98532	0.34	0.071407	5.24932	12.53589	
	O–Mn(IX)	2	1.98597	0.32	0.071407	5.25448	11.58347	
	O–Mn(X)	2	1.98904	0.32	0.071407	5.27888	11.49435	
	O–Mn(XI)	2	1.99018	0.35	0.071407	5.28797	12.84463	
	O–Mn(XII)	2	1.99083	0.34	0.071407	5.29315	12.36337	
	O–Tl(I)	2	2.28171	0.1	0.071407	7.9688	0.665 542	
	O–Tl(II)	2	2.30589	0.1	0.071407	8.22484	0.631 371	
	O–Tl(III)	2	2.33132	0.14	0.071407	8.49997	1.433 789	
	O–Tl(IV)	2	2.36947	0.12	0.071407	8.92412	0.936 555	
	O–Tl(V)	2	2.39337	0.12	0.071407	9.19689	0.890 718	
	O–Tl(VI)	2	2.41888	0.11	0.071407	9.49411	0.670 893	

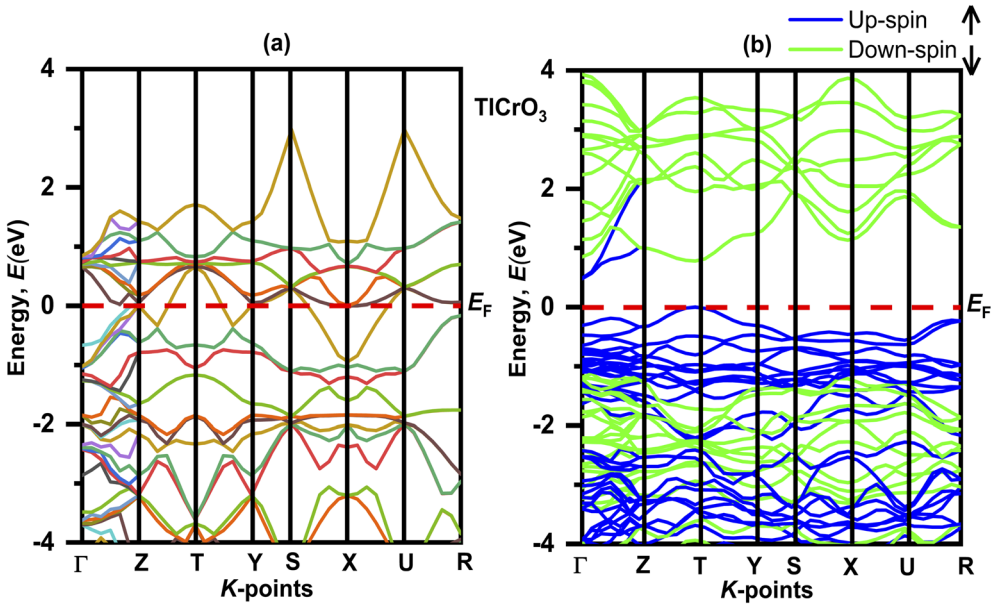

Fig. 4 Electronic band structure of $TlCrO_3$ (a) without spin and (b) with spin.

both $TlCrO_3$ and $TlMnO_3$, respectively, as no scattering of electrons can be seen along the Fermi level (E_F) for both the solids. These results showed the material $TlBO_3$ (B = Cr, Mn) switching from metallic to semiconductor nature. These are very much promising results that can be used to explain the metallic and optoelectronics properties, which may result from both Cr and Mn being magnetic atoms.[103,104] No previous study on the density of states and band structure has been done.

The evaluated total (TDOS) and partial density of states (PDOS) of $TlCrO_3$ without spin and with spin along with atomic contributions of different orbitals around E_F by the CASTEP code are displayed in Fig. 6(a) and (b), respectively. Also, the total (TDOS) and partial density of states (PDOS) of $TlMnO_3$ without spin and with along with the atomic contributions of different orbitals around the Fermi level are displayed in Fig. 7(a) and (b), correspondingly. In Fig. 6(a) and 7(a), the E_F of the TDOS without spin values are about 10 and 24 states/eV for $TlCrO_3$ and $TlMnO_3$, respectively. For both the materials, the Tl-3p orbital seems to be contribute to both the valence band and conduction band. $TlCrO_3$ contributes to both bands in case of Tl-3p orbital at ~−0.7 eV (~3.3 states per eV) and ~0.13 eV (3.7 states per eV). $TlMnO_3$ contributes ~−0.6 eV (~1.7 states/eV) and ~1.6 eV (~2.4 states per eV). $TlCrO_3$ contributes more to the formation of both the conduction and valence bands, resulting in less overlap of both the bands. As a result, $TlCrO_3$ is less metallic. It can be observed from Fig. 6(a) and 7(a) that major contribution near the Fermi

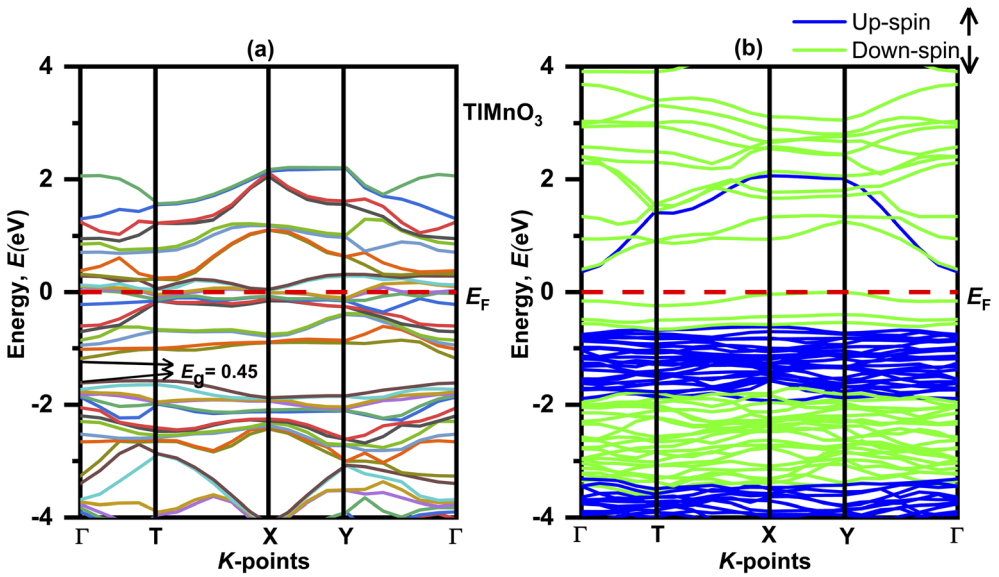

Fig. 5 Electronic band structure of $TlMnO_3$ (a) without spin and (b) with spin.

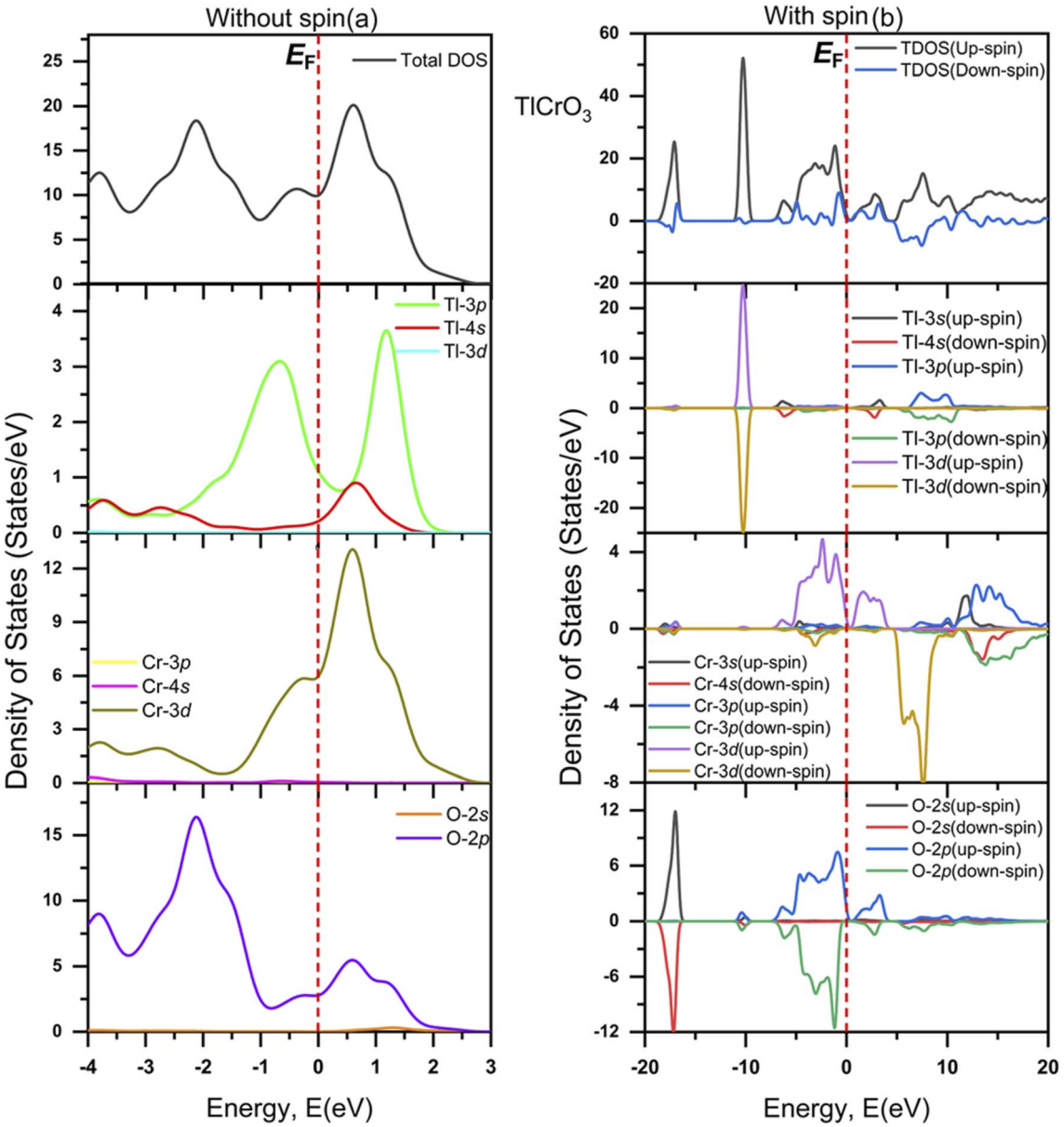

Fig. 6 Total and partial DOS of $TlCrO_3$ (a) without spin and (b) with spin.

level (E_F) is derived from Cr-3d and Mn-3d. Here, Cr-3d seems to contribute more to the formation of the conduction band at ~0.6 eV. However, Mn-3d contributes along the Fermi level, making $TlMnO_3$ more metallic. Both $TlCrO_3$ and $TlMnO_3$ compounds also have a fair contribution along with E_F from the O-2p orbital. The orbitals also seem to have significant overlaps in energy without spin, which point toward hybridization and inclination to the creation of covalent bonding. The values of DOS are finite, which indicates $TlBO_3$ (B = Cr, Mn) to be metallic. Moreover, the O-2p contributes to the creation of the valence band at ~−2.1 eV (for $TlCrO_3$) and ~−2.2 eV (for $TlMnO_3$) below the Fermi level (E_F). Hence, both perovskite materials are metallic. Two TDOS peaks for $TlMnO_3$ are found with close values at ~−2.1 eV and 0.7 eV. $TlMnO_3$ has the largest TDOS peak at E_F, again confirming it to have more metallic characteristics. In case of density of states without spin that is displayed in Fig. 6(a) and with spin displayed in Fig. 6(b), the value of TDOS along the E_F level is ~10 eV and ~2 (both up-spin and down-spin), respectively. For $TlMnO_3$, the value of TDOS along the E_F level is ~24 in case of without spin (Fig. 7(a)) and ~1 (both up-spin and down-spin) with spin (Fig. 7(b)).

3.6 Optical properties

These properties are important for describing the response of solids to an electromagnetic wave and for exploring the potential of photovoltaic and optoelectronic devices. In this context, the performances of the materials to the infrared, visible, and ultraviolet light are particularly noteworthy. Various optical energy-dependent (frequency) parameters, which are the absorption co-efficient $\alpha(\omega)$, conductivity $\sigma(\omega)$, reflectivity $R(\omega)$,

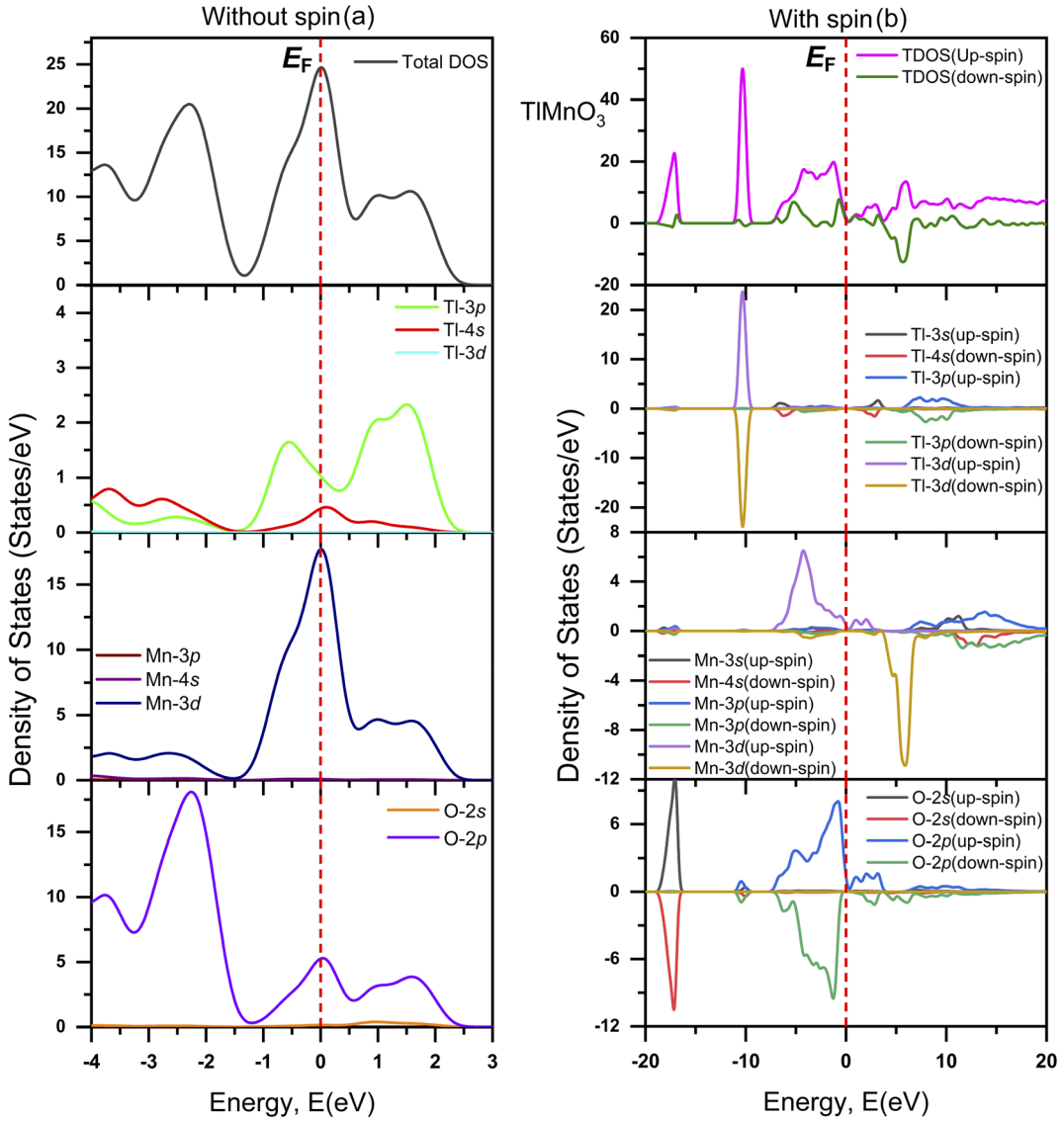

Fig. 7 Total and partial DOS of $TlMnO_3$ (a) without spin and (b) with spin.

the real part of dielectric function $\varepsilon(\omega)$, loss function $L(\omega)$, and the refractive index $n(\omega)$ are calculated for photon energies up to 50 eV with electric field polarization vectors along the [100] direction to analyze $TlBO_3$ (B = Cr, Mn). Fig. 8 and 9 depicted the different optical properties. The absorption spectrum without spin and with spin is displayed in Fig. 8(a) and (d), which shows expansion at inferior energies from ~0 to 15 eV in case of without spin due to transitions between close-lying energy levels, including the band. Absorption with spin shows a drastic change, which shows expansion of absorption from ~2 eV to ~36 eV. With spin, both materials exhibit possible application as photovoltaic cells.

The peaks associated with the interband transitions exist in the optical conductivity spectrum, which is presented in Fig. 8(b) (without spin) and 8(e) (with spin). A sharp edge can be seen for $TlMnO_3$ near the UV region ~2 eV and expansion can be seen for $TlCrO_3$ near ~4 eV in Fig. 8(b) without spin. However, in the case of with spin in Fig. 8(e), expansion can be seen in conductivity from 0 eV to ~36 eV. This suggests the electrical conductivity in both the materials. Though the peak value is lower than that without spin, it shows a steady peak value rather than a sharp peak. The reflectivity is presented in Fig. 8(c) (without spin) and 8(e) (with spin) for both $TlCrO_3$ and $TlMnO_3$. The zero-frequency reflectivity ($R(0)$) in Fig. 8(c) is ~0.47 and ~0.71 for $TlCrO_3$ and $TlMnO_3$, respectively, but it decreases when evaluated with spin in Fig. 8(f). The zero-frequency reflectivity ($R(0)$) in Fig. 8(f) is only is ~0.0.26 and ~0.28 for $TlCrO_3$ and $TlMnO_3$, respectively. A minor peak in the high-energy region is produced for $TlCrO_3$ due to interband carriers.

We considered the optical properties in the interband region. Dielectric function $\varepsilon(\omega)$ is generally measured by the interband along with interband optical transitions. For this investigation, we overlooked the indirect intraband transition as this comprises phonon with an inadequate scattering cross-section compared to that of direct transition; as a result, phonon scattering is not required to recollect the momentum. The $\varepsilon(0)$ static

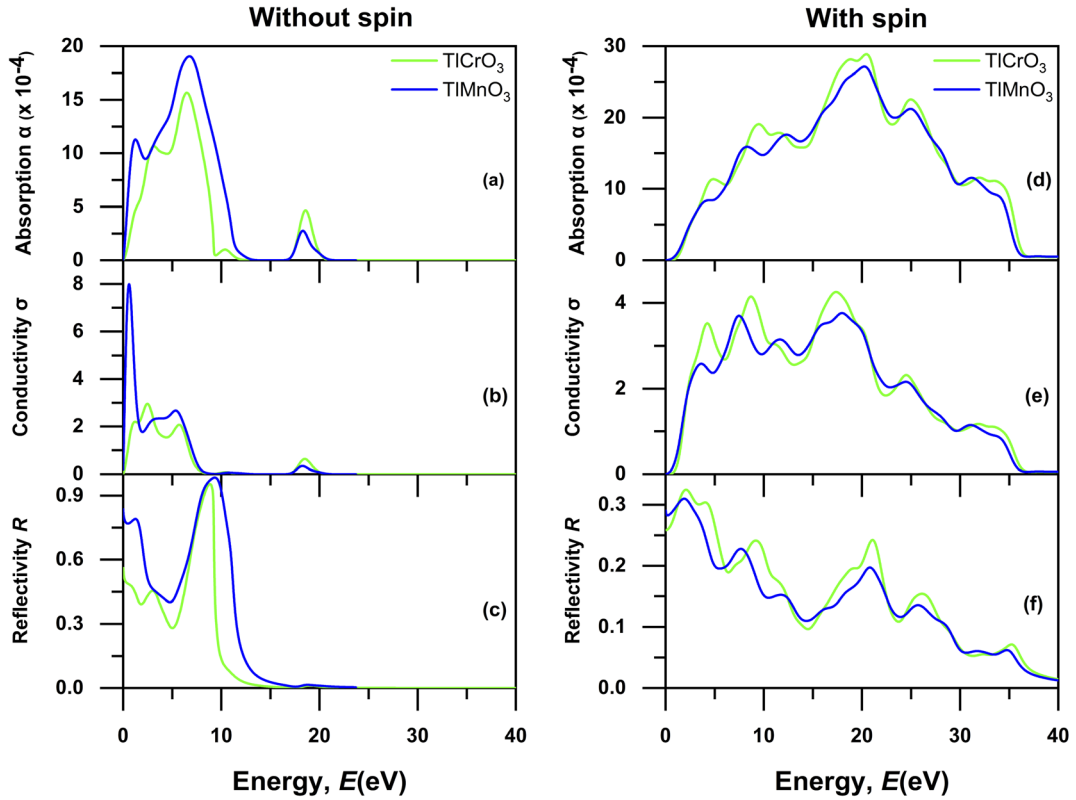

Fig. 8 Energy-dependent absorption $\alpha(\omega)$, conductivity $\sigma(\omega)$, and reflectivity $R(\omega)$ of $TlBO_3$ (B = Cr, Mn) without spin (a–c) and with spin (d–f).

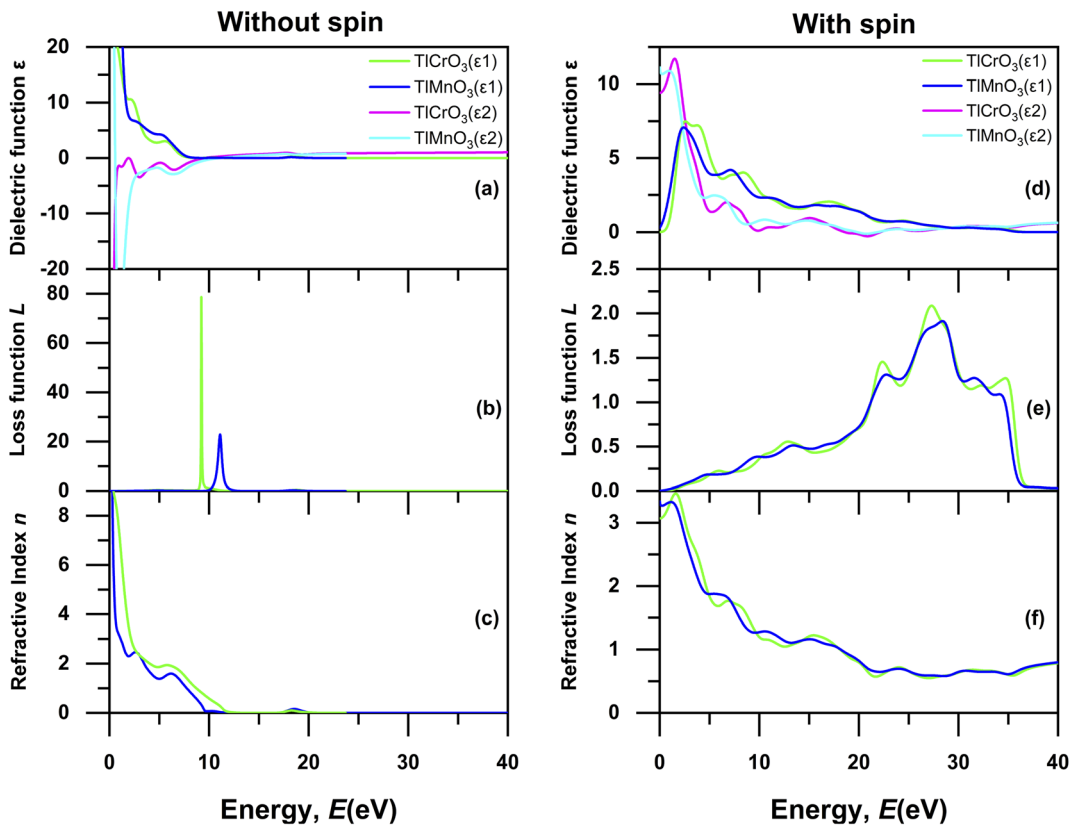

Fig. 9 Energy-dependent dielectric function $\varepsilon(\omega)$ (ε_1 real and ε_2 imaginary), loss function $L(\omega)$, and refractive index $n(\omega)$ of $TlBO_3$ (B = Cr, Mn) without spin (a–c) and with spin (d–f).

Table 6 The calculated density (ρ), longitudinal, transverse, and average sound velocities (v_l, v_t, and v_m), Debye temperature (θ_D), melting temperature (T_m), and minimum thermal conductivity (K_{min}) of the $TlBO_3$ (B = Cr, Mn) compound

Compounds	Crystal systems	ρ (g cm^{-3})	v_l (km s^{-1})	v_t (km s^{-1})	v_m (km s^{-1})	θ_D (K)	T_m (K)	K_{min} (W m^{-1} K^{-1})
$TlCrO_3$	Orthorhombic	8.898	4.319	2.772	3.045	403.5	1697.53	0.83
$TlMnO_3$	Triclinic	8.982	3.898	2.514	2.760	365.7	1544.35	0.75

dielectric constant is a significant optical parameter that is related to the semiconductor optical band gap and sometimes displays an opposite relationship with the values of the bandgap. Fig. 9(a) and (d) represent the energy loss function without spin and with spin, respectively, which means the loss of a fast-moving electron passing through the solid. The maximum energy loss of $TlCrO_3$ and $TlMnO_3$ in case of without spin occurs at ~9 eV and ~12 eV, respectively. The energy related to the peak is called the plasma peak and the related frequency is named plasma frequency. Moreover, if more energy compared to plasma frequency is generated, the investigated materials would develop transparency. Nevertheless, when the loss function of both the solids is evaluated with spin, the value of loss function is decreased and both display similar expansion from 0 eV to 40 eV. The optical property, *viz.*, the refractive index, holds a significant role from the standpoint of applications such as solar cells, photonic crystals, and waveguides. The calculated values of the zero-frequency refractive index are ~9 and ~10 for the solids $TlCrO_3$ and $TlMnO_3$, respectively, as shown in Fig. 9(c) in case of without spin. As the frequency is increased more than 10 eV, the values of the refractive index decrease for both the materials, and slight non-linear nature can also be seen. In Fig. 9(f) with spin, the value of the refractive index decreases to ~3 and ~3.3 for $TlCrO_3$ and $TlMnO_3$, respectively.

3.7 Thermodynamic properties

The thermodynamic properties of $TlBO_3$ (B = Cr, Mn) are significant to find different natures of the solids under different pressures and temperatures. Different variety of thermodynamic properties can be measured such as Debye temperature (θ_D), melting temperature (T_m), and minimum thermal conductivity (K_{min}) using other properties such as density (ρ), longitudinal, transverse, and average sound velocities (v_l, v_t, and v_m). The Debye temperature (θ_D) is evaluated as follows.[105]

$$\theta_D = \frac{h}{k_B}\left[\frac{3m}{4\pi}\left(\frac{N_A\rho}{M}\right)\right]^{\frac{1}{3}} v_m \quad (27)$$

where h, k_B, V, v_m, and n is Planck's constant, Boltzmann constant, unit cell volume, average sound velocity, and the number of atoms in the unite cell, respectively. Here, v_m can be evaluated by the equation

$$v_m = \left[\frac{1}{3}\left(\frac{2}{{v_t}^3} + \frac{1}{{v_l}^3}\right)\right]^{-1/3} \quad (28)$$

where v_l is the transverse velocity and v_t is the longitudinal sound velocity of the solids. v_l and v_t are evaluated by the formula below.

$$v_l = \left(\frac{B + \frac{4}{3}G}{\rho}\right) \quad (29)$$

$$v_t = \left[\frac{G}{\rho}\right]^{1/2} \quad (30)$$

The melting temperature (T_m) is also determined to explore the possible application of the materials at high temperatures. The following equation is used to determine (T_m).[106]

$$T_m = 354 + \frac{4.5(2C_{11} + C_{33})}{3} \quad (31)$$

Thermal conductivity, an important parameter to investigate the heat conduction of both $TlCrO_3$ and $TlMnO_3$, was determined. The minimum thermal conductivity (K_{min}) of a solid material is associated with temperature and will decrease to a certain value with a steady rise in temperature.[107] Minimum thermal conductivity (K_{min}) is calculated by Clarke formula.[108]

$$K_{min} = k_B v_m \left(\frac{M}{\rho N_A n}\right)^{-2/3} \quad (32)$$

where M, n, and N_A signify the molecular mass, atoms per molecule, and Avogadro's number, respectively. The calculated thermal properties θ_D,T_m, K_{min}, v_m, v_t, and v_l are presented in Table 6. The values of θ_D and K_{min} for the title compounds are much lower than the commercialized thermal barrier coating (TBC) compound $Y_4Al_{12}O_9$ (K_{min} = 1.13 W m^{-1} K^{-1}; θ_D = 564 K).[109,110]

4. Conclusions

The physical properties such as structural, mechanical, elastic anisotropic, Vickers hardness, electronic, optical, and thermodynamic properties of $TlBO_3$ (B = Cr, Mn) structured perovskites were investigated for the first time using *ab initio*-based DFT calculations. Good agreement was obtained between the calculated values and the obtained elastic constants. Born criteria for both the materials was fulfilled, signifying that both solids are mechanically stable. Both materials are ductile, as defined by all the elastic moduli such as Cauchy pressure, Poisson's ratio, and Pugh's ratio. All the different methods employed for studying the anisotropy of $TlBO_3$ (B = Cr, Mn) obtained the same results. The hardness calculations reveal that both solids are flexible, soft, and suitable for making a thin film. The Vickers hardness value is also very small compared to MAX phase materials. Both solids displayed a transition from

metallic to semiconducting nature without spin and with spin configuration. The investigation of the optical properties of both $TlCrO_3$ and $TlMnO_3$ reveals various possible uses such as waveguides, ultralarge integration of integrated circuits, microelectronics, and the reduction of solar heating, where the investigation with spin study exposes both materials' better absorption and application in solar cells. The solids have lower values of θ_D and K_{min}, which implies that they can be used as a thermal barrier coating (TBC) material. We hope that this investigation will help a researcher use these materials for different applications according to their physical properties and inspire scientists both experimentally and theoretically to discover this material in more depth in the future.

Data availability

All data needed to evaluate the conclusion of this study are presented in the paper. Additional data are available from the corresponding author upon reasonable request.

Author contributions

Wakil Hasan: methodology, data curation, formal analysis, writing original draft; Adeeb Mahamud Hossain: formal analysis, review-editing; Md. Rasheduzzaman: conceptualization, supervision, formal analysis, review-editing. Md. Atikur Rahman: validation, formal analysis, review-editing; Md. Mukter Hossain: formal analysis, review-editing; supervision, K. Rashel Mohammad: formal analysis, review-editing; Raihan Chowdhury: formal analysis, review-editing; Khandaker Monower Hossain: formal analysis, review-editing; M. Moazzam Hossen: formal analysis, review-editing; Md. Zahid Hasan: investigation, conceptualization, supervision, formal analysis, review-editing.

Conflicts of interest

The authors declare no conflict of interests.

Acknowledgements

Authors are grateful to the Department of Physics, Chittagong University of Engineering & Technology (CUET), Chattogram-4349 and Department of Physics, Pabna University of Science and Technology, Pabna-6600, Bangladesh, for providing the computing facilities for this work.

References

1 J. B. MacChesney, J. J. Jetzt, J. F. Potter, H. J. Williams and R. C. Sherwood, *J. Am. Ceram. Soc.*, 1966, **49**, 644–647.
2 M. E. Lines, A. M. Glass and G. Burns, *Phys. Today*, 1978, **31**, 56–58.
3 G. Banach and W. M. Temmerman, *Phys. Rev. B: Condens. Matter Mater. Phys.*, 2004, **69**, 054427.
4 S. Mathi Jaya, R. Jagadish, R. S. Rao and R. Asokamani, *Phys. Rev. B: Condens. Matter Mater. Phys.*, 1991, **43**, 13274–13279.
5 L. F. Mattheiss, *Phys. Rev. B: Solid State*, 1972, **5**, 290–306.
6 N. F. Quackenbush, J. W. Tashman, J. A. Mundy, S. Sallis, H. Paik, R. Misra, J. A. Moyer, J.-H. Guo, D. A. Fischer, J. C. Woicik, D. A. Muller, D. G. Schlom and L. F. J. Piper, *Nano Lett.*, 2013, **13**, 4857–4861.
7 E. Dagotto, *Science*, 2005, **309**, 257–262.
8 A. V. Boris, Y. Matiks, E. Benckiser, A. Frano, P. Popovich, V. Hinkov, P. Wochner, M. Castro-Colin, E. Detemple, V. K. Malik, C. Bernhard, T. Prokscha, A. Suter, Z. Salman, E. Morenzoni, G. Cristiani, H.-U. Habermeier and B. Keimer, *Science*, 2011, **332**, 937–940.
9 T.-H. Kim, M. Angst, B. Hu, R. Jin, X.-G. Zhang, J. F. Wendelken, E. W. Plummer and A.-P. Li, *Proc. Natl. Acad. Sci. U. S. A.*, 2010, **107**, 5272–5275.
10 C. Giannetti, M. Capone, D. Fausti, M. Fabrizio, F. Parmigiani and D. Mihailovic, *Adv. Phys.*, 2016, **65**, 58–238.
11 M. Imada, A. Fujimori and Y. Tokura, *Rev. Mod. Phys.*, 1998, **70**, 1039–1263.
12 J. Zaanen, G. A. Sawatzky and J. W. Allen, *Phys. Rev. Lett.*, 1985, **55**, 418–421.
13 K. Held, G. Keller, V. Eyert, D. Vollhardt and V. I. Anisimov, *Phys. Rev. Lett.*, 2001, **86**, 5345–5348.
14 Z. Shen and D. Dessau, *J. Phys. C: Solid State Phys.*, 1972, **5**, 1253.
15 S. Nakamura, K. Nanba and S. Iida, *J. Magn. Magn. Mater.*, 1998, **177–181**, 884–885.
16 B. C. H. Steele and A. Heinzel, in *Materials for Sustainable Energy*, Co-Published with Macmillan Publishers Ltd, UK, 2010, pp. 224–231.
17 A. J. Jacobson, *Chem. Mater.*, 2010, **22**, 660–674.
18 T. Wolfram and S. Ellialtioglu, *Electronic and optical properties of D-band perovskites*, Cambridge University Press, Cambridge, UK, New York, 2006.
19 Z. Feng, H. Hu, S. Cui and C. Bai, *Solid State Commun.*, 2008, **148**, 472–475.
20 S.-J. Kim, G. Demazeau, J. A. Alonso and J.-H. Choy, *J. Mater. Chem.*, 2001, **11**, 487–492.
21 Z. Ali, I. Ahmad, I. Khan and B. Amin, *Intermetallics*, 2012, **31**, 287–291.
22 S. Takeno, R. Ohara, K. Sano and T. Kawakubo, *Surf. Interface Anal.*, 2003, **35**, 29–35.
23 M. Yoshino, *Solid State Ionics*, 2000, **127**, 109–123.
24 Z. Fang, N. Nagaosa, K. S. Takahashi, A. Asamitsu, R. Mathieu, T. Ogasawara, H. Yamada, M. Kawasaki, Y. Tokura and K. Terakura, *Science*, 2003, **302**, 92–95.
25 J. F. Scott, *Science*, 2007, **315**, 954–959.
26 E. Cross, *Nature*, 2004, **432**, 24–25.
27 T. Schneider, D. Leduc, J. Cardin, C. Lupi, N. Barreau and H. Gundel, *Opt. Mater.*, 2007, **29**, 1871–1877.
28 R. Watton, *Ferroelectrics*, 1989, **91**, 87–108.
29 R. D. Shannon, *Inorg. Chem.*, 1967, **6**, 1474–1478.
30 A. A. Belik, Y. Matsushita, M. Tanaka and E. Takayama-Muromachi, *Chem. Mater.*, 2012, **24**, 2197–2203.
31 W. Yi, Y. Matsushita, Y. Katsuya, K. Yamaura, Y. Tsujimoto, I. A. Presniakov, A. V. Sobolev, Y. S. Glazkova, Y. O. Lekina, N. Tsujii, S. Nimori, K. Takehana, Y. Imanaka and A. A. Belik, *Dalton Trans.*, 2015, **44**, 10785–10794.

32 S. Niitaka, *Solid State Ionics*, 2004, **172**, 557–559.
33 C. Darie, C. Goujon, M. Bacia, H. Klein, P. Toulemonde, P. Bordet and E. Suard, *Solid State Sci.*, 2010, **12**, 660–664.
34 A. A. Belik, N. Tsujii, H. Suzuki and E. Takayama-Muromachi, *Inorg. Chem.*, 2007, **46**, 8746–8751.
35 A. V. Sobolev, A. V. Bokov, W. Yi, A. A. Belik, I. A. Presniakov and I. S. Glazkova, *J. Exp. Theor. Phys.*, 2019, **129**, 896–902.
36 K. Sardar, M. R. Lees, R. J. Kashtiban, J. Sloan and R. I. Walton, *Chem. Mater.*, 2011, **23**, 48–56.
37 T. Kimura, T. Goto, H. Shintani, K. Ishizaka, T. Arima and Y. Tokura, *Nature*, 2003, **426**, 55–58.
38 M. Fiebig, Th. Lottermoser, D. Fröhlich, A. V. Goltsev and R. V. Pisarev, *Nature*, 2002, **419**, 818–820.
39 Y. Kumagai, A. A. Belik, M. Lilienblum, N. Leo, M. Fiebig and N. A. Spaldin, *Phys. Rev. B: Condens. Matter Mater. Phys.*, 2012, **85**, 174422.
40 S. Lee, A. Pirogov, M. Kang, K.-H. Jang, M. Yonemura, T. Kamiyama, S.-W. Cheong, F. Gozzo, N. Shin, H. Kimura, Y. Noda and J.-G. Park, *Nature*, 2008, **451**, 805–808.
41 M. Tachibana, T. Shimoyama, H. Kawaji, T. Atake and E. Takayama-Muromachi, *Phys. Rev. B: Condens. Matter Mater. Phys.*, 2007, **75**, 144425.
42 V. Yu Pomjakushin, M. Kenzelmann, A. Dönni, A. B. Harris, T. Nakajima, S. Mitsuda, M. Tachibana, L. Keller, J. Mesot, H. Kitazawa and E. Takayama-Muromachi, *New J. Phys.*, 2009, **11**, 043019.
43 B. Rajeswaran, D. I. Khomskii, A. K. Zvezdin, C. N. R. Rao and A. Sundaresan, *Phys. Rev. B: Condens. Matter Mater. Phys.*, 2012, **86**, 214409.
44 C. R. Serrao, A. K. Kundu, S. B. Krupanidhi, U. V. Waghmare and C. N. R. Rao, *Phys. Rev. B*, 2005, **72**, 220101.
45 J.-S. Zhou, J. A. Alonso, V. Pomjakushin, J. B. Goodenough, Y. Ren, J.-Q. Yan and J.-G. Cheng, *Phys. Rev. B: Condens. Matter Mater. Phys.*, 2010, **81**, 214115.
46 T. Goto, T. Kimura, G. Lawes, A. P. Ramirez and Y. Tokura, *Phys. Rev. Lett.*, 2004, **92**, 257201.
47 Y. Tokunaga, S. Iguchi, T. Arima and Y. Tokura, *Phys. Rev. Lett.*, 2008, **101**, 097205.
48 A. Paul, A. Mukherjee, I. Dasgupta, A. Paramekanti and T. Saha-Dasgupta, *Phys. Rev. Lett.*, 2019, **122**, 016404.
49 W. Yi, Y. Kumagai, N. A. Spaldin, Y. Matsushita, A. Sato, I. A. Presniakov, A. V. Sobolev, Y. S. Glazkova and A. A. Belik, *Inorg. Chem.*, 2014, **53**, 9800–9808.
50 D. D. Khalyavin, P. Manuel, W. Yi and A. A. Belik, *Phys. Rev. B*, 2016, **94**, 134412.
51 A. A. Belik, *J. Solid State Chem.*, 2017, **246**, 8–15.
52 M. L. Keith and R. Roy, *Am. Mineral.*, 1954, **39**, 1–23.
53 R. S. ROTH, *J. Res. Natl. Bur. Stand.*, 1957, **58**, 75–88.
54 Z. Ali, I. Ahmad and A. H. Reshak, *Phys. B*, 2013, **410**, 217–221.
55 Z. Ali and I. Ahmad, *J. Electron. Mater.*, 2013, **42**, 438–444.
56 L. Feng, Z. Liu and Q. Liu, *Phys. B*, 2012, **407**, 2009–2013.
57 M. Rasheduzzaman, K. Monower Hossain and M. Z. Hasan, *Int. J. Mater. Res.*, 2020, **111**, 1038–1046.
58 M. Z. Hasan, M. Rasheduzzaman and K. Monower Hossain, *Chin. Phys. B*, 2020, **29**, 123101.
59 Md. Z. Hasan, K. M. Hossain, S. K. Mitro, Md. Rasheduzzaman, J. K. Modak and M. A. Rayhan, *Appl. Phys. A*, 2021, **127**, 36.
60 E. F. Bertaut, A. Delapalme, F. Forrat, G. Roult, F. De Bergevin and R. Pauthenet, *J. Appl. Phys.*, 1962, **33**, 1123–1124.
61 N. Shamir, H. Shaked and S. Shtrikman, *Phys. Rev. B: Condens. Matter Mater. Phys.*, 1981, **24**, 6642–6651.
62 C. V. Colin, A. G. Pérez, P. Bordet, C. Goujon and C. Darie, *Phys. Rev. B: Condens. Matter Mater. Phys.*, 2012, **85**, 224103.
63 G. Demazeau, A. Marbeuf, M. Pouchard and P. Hagenmuller, *J. Solid State Chem.*, 1971, **3**, 582–589.
64 S. J. Kim, G. Demazeau, J. A. Alonso, A. Largeteau, J. M. Martinez-Lope, I. Presniakov and J.-H. Choy, *Solid State Commun.*, 2000, **117**, 113–115.
65 Y. Cao, S. Cao, W. Ren, Z. Feng, S. Yuan, B. Kang, B. Lu and J. Zhang, *Appl. Phys. Lett.*, 2014, **104**, 232405.
66 M. Itoh, J. Hashimoto, S. Yamaguchi and Y. Tokura, *Phys. B*, 2000, **281–282**, 510–511.
67 L. Ding, P. Manuel, D. D. Khalyavin, F. Orlandi, Y. Kumagai, F. Oba, W. Yi and A. A. Belik, *Phys. Rev. B*, 2017, **95**, 054432.
68 S. Clark and M. Segall, *Z. Kristallogr.*, 2005, **220**, 567.
69 J. P. Perdew, A. Ruzsinszky, G. I. Csonka, O. A. Vydrov, G. E. Scuseria, L. A. Constantin, X. Zhou and K. Burke, *Phys. Rev. Lett.*, 2009, **102**, 039902.
70 P. Hohenberg and W. Kohn, *Phys. Rev.*, 1964, **136**, B864–B871.
71 M. D. Segall, P. J. D. Lindan, M. J. Probert, C. J. Pickard, P. J. Hasnip, S. J. Clark and M. C. Payne, *J. Phys.: Condens. Matter*, 2002, **14**, 2717–2744.
72 H. J. Monkhorst and J. D. Pack, *Phys. Rev. B: Solid State*, 1976, **13**, 5188–5192.
73 B. G. Pfrommer, M. Côté, S. G. Louie and M. L. Cohen, *J. Comput. Phys.*, 1997, **131**, 233–240.
74 C.-Z. Fan, S.-Y. Zeng, L.-X. Li, Z.-J. Zhan, R.-P. Liu, W.-K. Wang, P. Zhang and Y.-G. Yao, *Phys. Rev. B: Condens. Matter Mater. Phys.*, 2006, **74**, 125118.
75 R. Gaillac, P. Pullumbi and F.-X. Coudert, *J. Phys.: Condens. Matter*, 2016, **28**, 275201.
76 Y. R. Li, Z. T. Hou, T. X. Wang, Y. Li, H. Y. Liu, X. F. Dai and G. D. Liu, *J. Phys.: Conf. Ser.*, 2017, **827**, 012015.
77 R. Majumder and M. M. Hossain, *Comput. Condens. Matter*, 2019, **21**, e00402.
78 C. Truesdell, *Bull. Am. Math. Soc.*, 1952, **58**, 577–579.
79 J. Wang, S. Yip, S. R. Phillpot and D. Wolf, *Phys. Rev. Lett.*, 1993, **71**, 4182–4185.
80 D. C. Wallace, *Thermodynamics of Crystals. XVIII u. 484 S. mit 57 Abb.*, John Wiley & Sons Ltd., Chichester, New York, Sydney, Tokio, Mexiko, 1972.
81 H. Qin, B.-L. Yan, M. Zhong, C.-L. Jiang, F.-S. Liu, B. Tang and Q.-J. Liu, *Phys. B*, 2019, **552**, 151–158.
82 D. H. Chung and W. R. Buessem, *J. Appl. Phys.*, 1967, **38**, 2010–2012.
83 X. Gao, Y. Jiang, R. Zhou and J. Feng, *J. Alloys Compd.*, 2014, **587**, 819–826.
84 P. Ravindran, L. Fast, P. A. Korzhavyi, B. Johansson, J. Wills and O. Eriksson, *J. Appl. Phys.*, 1998, **84**, 4891–4904.

85 W. Voigt, *Lehrbuch Der Kristallphysik*, Vieweg + Teubner Verlag, Wiesbaden, 1966.
86 A. Reuss, *Z. Angew. Math. Mech.*, 1929, **9**, 49–58.
87 R. Hill, *Proc. Phys. Soc. A*, 1952, **65**, 349–354.
88 J. Maibam, B. Indrajit Sharma, R. Bhattacharjee, R. K. Thapa and R. K. Brojen Singh, *Phys. B*, 2011, **406**, 4041–4045.
89 S. F. Pugh, *Lond. Edinb. Dublin philos. mag. j. sci.*, 1954, **45**, 823–843.
90 Md. L. Ali and Md. Z. Rahaman, *Int. J. Mod. Phys. B*, 2018, **32**, 1850121.
91 D. G. Pettifor, *Mater. Sci. Technol.*, 1992, **8**, 345–349.
92 T. Ahmed, M. Roknuzzaman, A. Sultana, A. Biswas, Md. S. Alam, M. Saiduzzaman and K. M. Hossain, *Mater. Today Commun.*, 2021, **29**, 102973.
93 M. H. K. Rubel, K. M. Hossain, S. K. Mitro, M. M. Rahaman, M. A. Hadi and A. K. M. A. Islam, *Mater. Today Commun.*, 2020, **24**, 100935.
94 R. Majumder, S. K. Mitro and B. Bairagi, *J. Alloys Compd.*, 2020, **836**, 155395.
95 C. M. Kube, *AIP Adv.*, 2016, **6**, 095209.
96 A. Gueddouh, B. Bentria and I. K. Lefkaier, *J. Magn. Magn. Mater.*, 2016, **406**, 192–199.
97 H. Gou, L. Hou, J. Zhang and F. Gao, *Appl. Phys. Lett.*, 2008, **92**, 241901.
98 F. Gao, *Phys. Rev. B: Condens. Matter Mater. Phys.*, 2006, **73**, 132104.
99 M. A. Ali, M. A. Hadi, M. M. Hossain, S. H. Naqib and A. K. M. A. Islam, *Phys. Status Solidi B*, 2017, **254**, 1700010.
100 A. Chowdhury, M. A. Ali, M. M. Hossain, M. M. Uddin, S. H. Naqib and A. K. M. A. Islam, *Phys. Status Solidi B*, 2018, **255**, 1700235.
101 M. I. Kholil, M. S. Ali and M. Aftabuzzaman, *J. Alloys Compd.*, 2018, **740**, 754–765.
102 P. Barua, M. M. Hossain, M. A. Ali, M. M. Uddin, S. H. Naqib and A. K. M. A. Islam, *J. Alloys Compd.*, 2019, **770**, 523–534.
103 H. Luo, Z. Zhu, L. Ma, S. Xu, H. Liu, J. Qu, Y. Li and G. Wu, *J. Phys. D: Appl. Phys.*, 2007, **40**, 7121–7127.
104 R. Fruchart, A. Roger and J. P. Senateur, *J. Appl. Phys.*, 1969, **40**, 1250–1257.
105 O. L. Anderson, *J. Phys. Chem. Solids*, 1963, **24**, 909–917.
106 M. E. Fine, L. D. Brown and H. L. Marcus, *Scr. Metall.*, 1984, **18**, 951–956.
107 Y. Shen, D. R. Clarke and P. A. Fuierer, *Appl. Phys. Lett.*, 2008, **93**, 102907.
108 D. R. Clarke, *Surf. Coat. Technol.*, 2003, **163–164**, 67–74.
109 M. H. K. Rubel, M. A. Hadi, M. M. Rahaman, M. S. Ali, M. Aftabuzzaman, R. Parvin, A. K. M. A. Islam and N. Kumada, *Comput. Mater. Sci.*, 2017, **138**, 160–165.
110 Y. Zhou, H. Xiang, X. Lu, Z. Feng and Z. Li, *J. Adv. Ceram.*, 2015, **4**, 83–93.